

Daughter bubble cascades produced by folding of ruptured thin films

James C. Bird¹, Riëlle de Ruiter¹, Laurent Courbin² & Howard A. Stone^{1,3}

Thin liquid films, such as soap bubbles, have been studied extensively for over a century because they are easily formed and mediate a wide range of transport processes in physics, chemistry and engineering^{1–3}. When a bubble on a liquid–gas or solid–gas interface (referred to herein as an interfacial bubble) ruptures, the general expectation is that the bubble vanishes. More precisely, the ruptured thin film is expected to retract rapidly until it becomes part of the interface, an event that typically occurs within milliseconds^{4–6}. The assumption that ruptured bubbles vanish is central to theories on foam evolution⁷ and relevant to health⁸ and climate⁹ because bubble rupture is a source for aerosol droplets^{10,11}. Here we show that for a large range of fluid parameters, interfacial bubbles can create numerous small bubbles when they rupture, rather than vanishing. We demonstrate, both experimentally and numerically, that the curved film of the ruptured bubble can fold and entrap air as it retracts. The resulting toroidal geometry of the trapped air is unstable, leading to the creation of a ring of smaller bubbles. The higher pressure associated with the higher curvature of the smaller bubbles increases the absorption of gas into the liquid, and increases the efficiency of rupture-induced aerosol dispersal.

A bubble-bursting cascade is illustrated experimentally in Fig. 1a–d. A hemispherical soap bubble, approximately four centimetres in diameter, is formed on a glass slide. Following rupture, a ring of smaller bubbles, each approximately a millimetre in diameter, appears around the base of the initial bubble (Fig. 1b). When one of these daughter bubbles ruptures, a ring of even smaller bubbles forms (Fig. 1d). Thus we observe a two-stage cascade, whereby one large bubble generates many smaller bubbles and so reduces the characteristic length scale over two orders of magnitude.

We believe that the physics responsible for this cascade generalizes beyond soap bubbles and provides an explanation for why, in the ocean, smaller bubbles are often observed after a larger sea bubble ruptures^{11,12}. The importance of daughter bubbles for aerosol dispersion is highlighted in Fig. 1e–j. An air bubble is created on a pool of water collected from a local river (42.369° N, 71.122° W). Indigenous surfactants tend to be present in estuaries and oceans¹³; these natural surfactants stabilize the bubble, allowing a larger size and longer lifetime than would be observed with pure water. Eventually a hole nucleates on the bubble, causing the film to retract^{4–6,13–19} and exposing the dimpled air–liquid interface to atmospheric pressure (Fig. 1f). The curved interface relaxes and propels a jet of liquid upward^{10,20–23}. Around this jet is a ring of daughter bubbles (Fig. 1g). Within half a second, the daughter bubbles burst and propel droplets into the atmosphere (Fig. 1h–j). Thus, by forming numerous daughter bubbles, a single larger bubble significantly increases aerosol generation.

To examine how the daughter bubbles are formed, we film the collapse of the bubble with two synchronized high-speed cameras, one viewing from the side and the other from below (Fig. 2). The

bubble is formed from a moderately viscous water–glycerol–sodium dodecyl sulphate solution to slow down the dynamics and stabilize the retracting rim. The high-speed images reveal that the daughter bubbles form in two distinct steps, each with a characteristic timescale. In the first step, the film collapses and folds such that air is trapped (Fig. 2a). The timescale over which the film retracts (about 3 ms) is consistent with inertially dominated film retraction^{5,14}. In the second step, each torus of air becomes unstable and breaks up into a ring of daughter bubbles (Fig. 2b). This longer timescale (about 50 ms) is consistent with a capillary-driven phenomenon regulated by viscosity (see Supplementary Information).

From our observations in Fig. 2, we can understand the dynamics of the daughter bubble cascade. Prior to rupture, there is an equilibrium where capillary stresses on the curved surface are directed inward and are balanced by the outwardly directed bubble pressure. Once a hole nucleates in the thin film, the edge of the film retracts^{5,14,15}. The compressed gas equilibrates instantaneously, that is, the pressure difference between the interior gas and the ambient vanishes, which results in a net inward force along the film due to capillary effects (see Supplementary Information). Meanwhile, the inertia of the liquid in the film leads to an outward trajectory of the moving rim. The combination of capillarity and inertia produces a folding of the film that entraps a torus of air. The torus itself, like other cylindrical fluid interfaces, is unstable to small perturbations and reduces surface energy by breaking into numerous small bubbles^{3,24,25}. Provided that each of these smaller bubbles behaves similarly to the initial bubble, the process is iterative, creating a bubble-bursting cascade.

To test this mechanism for film folding, we next numerically simulated the film dynamics during retraction. Although retraction of planar films is well-studied, simulations capable of capturing the dynamics of curved films have not been studied systematically. Therefore, we developed a mathematical model of the inertial dynamics of a curved, retracting film (Supplementary Fig. 1). Our goal was to identify an elementary description that accurately reproduces the observed film dynamics. We assumed that the film thickness is initially uniform and that the resulting bubble collapse is axisymmetric. Following the formation of a hole in the film, the gas pressure inside the bubble equilibrates with the atmospheric pressure on a timescale of the order of 10 μ s, which is set by the speed of sound. Surface tension drives the resulting collapse of the liquid film, whereas the inertia of the film regulates the motion. The simulations based on this model reproduce qualitative features of the experiments, but lack important details. These details are recovered when the simulations incorporate the internal pressure that results when the collapsing film squeezes the gas through the opening hole (Supplementary Fig. 2). The resulting shapes (Fig. 3a) are quantitatively similar to those observed experimentally (Fig. 2a). The collapse time and the initial film folding are accurately captured by the simulations.

¹School of Engineering and Applied Sciences, Harvard University, Cambridge, Massachusetts 02138, USA. ²Institut de Physique de Rennes, UMR CNRS 6251, Campus Beaulieu, Université Rennes 1, 35042 Rennes, France. ³Department of Mechanical and Aerospace Engineering, Princeton University, Princeton, New Jersey 08544, USA.

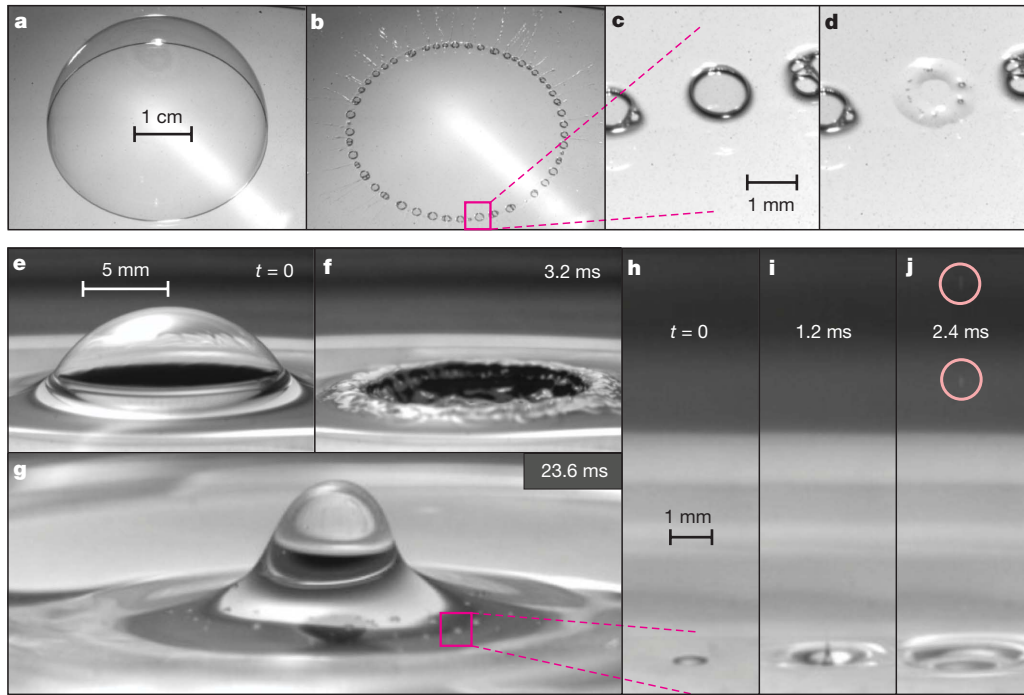


Figure 1 | The daughter bubble cascade, with jets, droplets and daughter bubbles resulting from bursting bubbles. **a–d**, When a single soap bubble ruptures on a rigid surface, a ring of many smaller bubbles can form. Similarly, when one of the daughter bubbles pops, even smaller bubbles are created, demonstrating a bubble-bursting cascade. **e**, The dynamics are more intricate when an air bubble ruptures on a deep pool of water. The Laplace pressure inside the bubble dimples the interface to create a cavity. **f**, Once the

bubble ruptures, the film rapidly retracts (within a time $t = 3.2$ ms). **g**, As the cavity re-equilibrates, a jet of liquid is propelled upward. Many smaller daughter bubbles are visible around the jet. **h–j**, Within a fraction of a second, these secondary bubbles burst (**h**), a narrow jet forms (**i**), and tiny liquid droplets are dispersed into the atmosphere (**j**, inside pink circles). For more detail, see Supplementary Movies 1 and 2.

During the final moments of the collapse, it appears that the film can trap two separate pockets of air by folding on the lower surface and folding back on itself (Fig. 3b). The consequence of this folding is visible in Fig. 2b, where close inspection reveals the break-up of two rings of air that are concentric when viewed from above. If the rim of the film is unstable during retraction, the rim is observed to form threads and small drops, allowing the air to escape when the film folds onto itself (Fig. 3c). In this case, only one ring of daughter bubbles is produced, as experimentally demonstrated in Fig. 1b.

From our observations and simulations, we conclude that there are three conditions that control how much gas is entrapped in daughter bubbles produced by a bursting bubble: (1) the ability of the film to bend inward as it retracts, (2) the stability of the rim, and (3) the energy required to displace the initial gas inside the bubble. Our simulations demonstrate that the retraction of the film needs to be underdamped for the film to bend inward. Thus we expect daughter bubbles to form only when the inertial effects in the film are greater than the viscous effects, corresponding to a Reynolds number

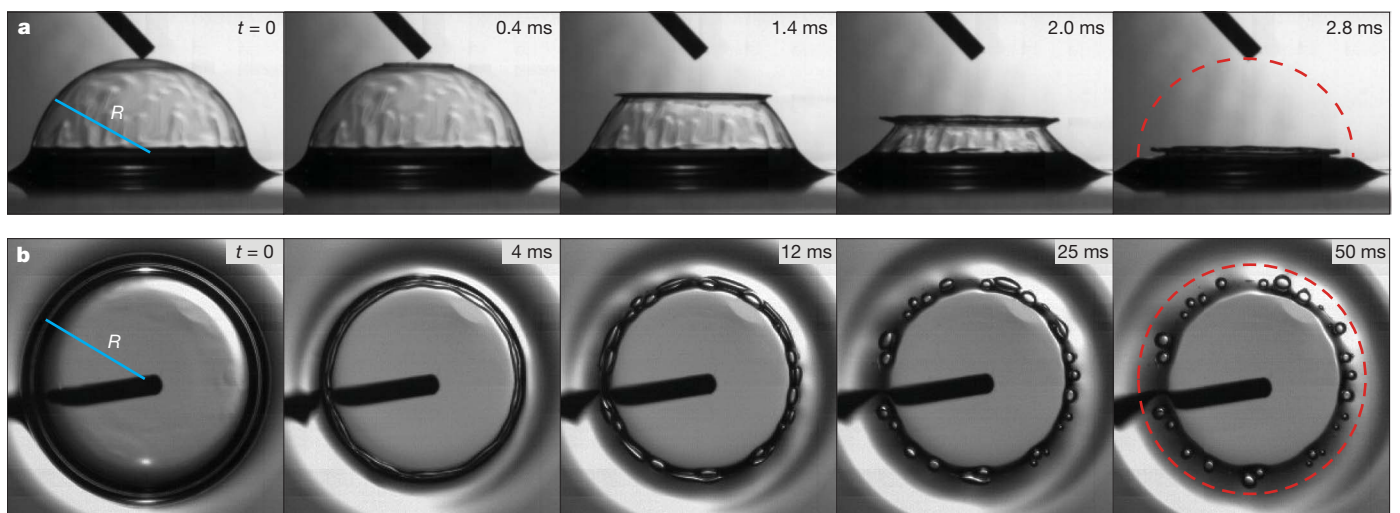


Figure 2 | Two-step mechanism to form daughter bubbles. **a**, High-speed images of a glycerol–water bubble filled with air popping on a solid surface viewed from the side. The bubble has an initial radius $R = 5.3$ mm, dynamic viscosity $\mu = 0.31$ Pa s, surface tension $\gamma = 55$ mN m⁻¹, and density $\rho = 10^3$ kg m⁻³. **b**, The rupture is simultaneously filmed from below and

reveals two concentric tori that break up into daughter bubbles. The red dotted lines in the final images denote the position of the bubble before rupture, and the time from rupture t is reported in milliseconds. For more detail, see Supplementary Movie 3.

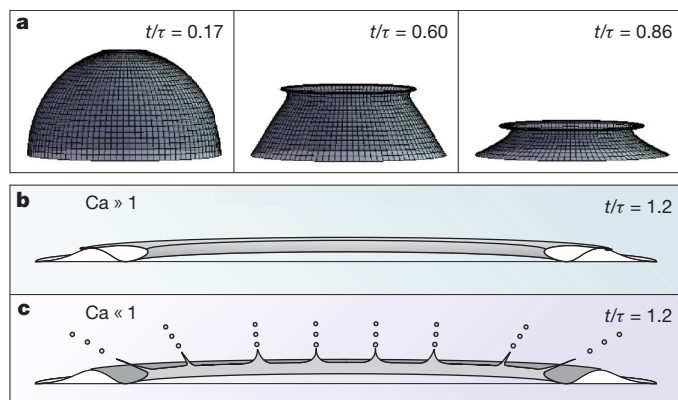


Figure 3 | Numerical simulations for understanding film folding and air entrapment. **a**, Our numerical simulation reproduces the inward folding behaviour of the collapsing film. The elapsed time t is dimensionalized by $\tau \equiv \sqrt{\rho R^2 h / \gamma}$. The selected times correspond to those in the three middle images in Fig. 2a with a film thickness of $h = 11 \mu\text{m}$. **b**, A cross-sectional schematic of the proposed folding during the last stages of the collapse demonstrates how the film can create two concentric rings of air by intersecting with itself and the lower interface. This situation occurs when the capillary number is large $Ca \equiv U\mu/\gamma \gg 1$. **c**, Another schematic illustrates how when the rim is unstable, the film traps only one torus of air. This rim instability appears to occur when $Ca \ll 1$.

$Re = \rho RU/\mu \gg 1$, where ρ is the liquid density, R is the bubble radius, U is the characteristic retraction speed of the film (as measured experimentally), and μ is the liquid viscosity. The stability of the retracting rim depends on how the thickness of the film varies in the vicinity of the rim. Previously reported simulations for planar films find that the shape of the rim depends on both the Reynolds number and the capillary number, $Ca = U\mu/\gamma$, where γ is the surface tension between the liquid and gas¹⁷. Specifically, the rim of a planar retracting film forms a distinct neck when both $Ca \ll 1$ and $Re \gg 1$, a condition that may cause the rim to break into tendrils and droplets. The instability of the rim appears to reduce the number of air torii from two to one, and the tendrils may even interfere with the remaining torus of air as it breaks up into daughter bubbles. Finally, our simulations suggest that the relative inertia between the gas and the film, $\rho_g R/(\rho h)$, where ρ_g is the gas density and h is the film thickness, influences the extent that the film folds inward and might therefore influence the size of the daughter bubbles (see Supplementary Information).

To test these predictions, we studied a set of bubbles with varying radius R and viscosity of the liquid μ over an extensive range, over nine and four orders of magnitude for Re and Ca respectively (Fig. 4). We also varied the density of the inner gas by blowing bubbles with helium, nitrogen and carbon dioxide. Three outcomes were observed: no daughter bubbles, one ring of daughter bubbles or two concentric rings of daughter bubbles (Fig. 4). Only when $Re > 2$ are daughter bubbles observed, providing more evidence that inertial effects are critical to their formation. At sufficiently low Reynolds numbers, we observe an azimuthal instability in the collapsing film^{6,18}, yet this instability does not entrap air and no daughter bubbles are formed. Additionally, the transition between one and two rings occurs when $Ca \approx 2$, supporting our hypothesis for instability of the rim. The density of the gas inside the bubble does not affect the number of rings obtained (Fig. 4), but we have observed that the specific gas does influence the average size of the daughter bubbles within the rings (see Supplementary Information).

The positions of the points in the bubble-bursting diagram (Fig. 4) provide additional insight into the film dynamics. At high Reynolds numbers, when viscosity is negligible, a uniform film retracts at a constant speed^{3,14,15}: $U = \sqrt{2\gamma/(\rho h)}$. This expression provides an equation for the capillary number in terms of the Reynolds number, $Ca = (2R/h)Re^{-1}$. The data points follow this trend in the inertial

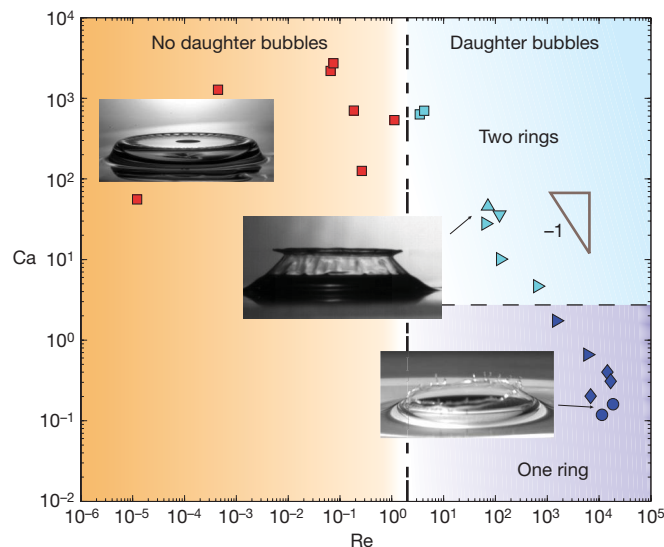


Figure 4 | Dynamical characterization of the formation of daughter bubbles. After a hemispherical bubble ruptures, there are either no daughter bubbles (red symbols), a single ring of daughter bubbles (blue symbols), or two concentric rings of daughter bubbles (cyan symbols). The transition between these regimes coincides with $Ca \equiv U\mu/\gamma$ and $Re \equiv \rho UR/\mu$ of approximately one, as predicted by our scaling arguments. The shapes of the data points correspond to various configurations: bubbles formed on deep pools of pure silicone oil (squares), on thin films of glycerol–water solutions stabilized by SDS surfactant (all triangles), and on deep pools of local river water stabilized by indigenous surfactant (circles and diamonds). The effects of different gases inside the bubbles were investigated using helium (right triangles and diamonds), nitrogen (up triangles), carbon dioxide (down triangles), and air (squares and circles).

regime with $2R/h \approx 1,000$ (Fig. 4). In contrast, when inertia is negligible ($Re \ll 1$), a uniform film retracts at an exponential rate with a characteristic speed¹⁶ $U \propto R\gamma/(h\mu)$, which implies that at low Reynolds numbers, the capillary number follows $Ca \propto R/h$. The dynamics are consistent with the data reported in the phase plot, and we attribute the slight scatter in Ca at low Re to variability in the relative film thickness. The transition between these two regimes ($Re \ll 1$ and $Re \gg 1$) coincides with the transition between no daughter bubbles and daughter bubbles (Fig. 4) and thus quantitatively rationalizes our observations.

Our results are relevant to the many fields that interfacial bubbles are already known to affect because we show that under certain conditions an initial bubble is a source for many smaller, more influential, bubbles. Aerosol droplets from bursting bubbles have been implicated in the transmission of diseases in swimming pools and hot tubs^{8,26}. On a larger scale, sea spray, which transports dissolved gases, salt, thermal energy, and biological materials to the atmosphere and therefore influences climate, is largely attributed to aerosols produced by an estimated 10^{18} to 10^{20} bubbles that rupture every second across the oceans^{9–11,27}. Before bursting, interfacial bubbles aerate the upper level of the ocean by increasing the adsorption of atmospheric gases into the water column²⁸. In addition, interfacial bubbles can be problematic in industry, such as in glass manufacturing where air bubbles must be removed before the glass solidifies²⁹, and in biotechnology where the rapid liquid acceleration produced by a bursting bubble has been linked to cell mortality³⁰. In these industrial processes where smaller bubbles, or the effects of small bubbles, are detrimental, understanding how these bubbles form is the first step in mitigation. We have quantified the limits of the folding behaviour and have shown that tuning the Reynolds and capillary numbers can suppress the formation of daughter bubbles. In situations where control of the interfacial properties is unrealistic, such as on the ocean surface, our study highlights the importance of larger bubbles in heat and mass exchange, as these bubbles can create many smaller bubbles each of which is capable of

dissolving gas into the water column and dispersing aerosols into the atmosphere.

Received 21 January; accepted 1 April 2010.

- de Gennes, P. G., Brochard-Wyart, F. & Quéré, D. *Capillarity and Wetting Phenomena* (Springer, 2004).
- Isenberg, C. *The Science of Soap Films and Soap Bubbles* (Dover Publications, 1978).
- Eggers, J. & Villermaux, E. Physics of liquid jets. *Rep. Prog. Phys.* **71**, 036601 (2008).
- Dupré, A. Sixième mémoire sur la théorie mécanique de la chaleur. *Ann. Chim. Phys.* **11**, 194–220 (1867).
- Taylor, G. I. The dynamics of thin sheets of fluid. III. Disintegration of fluid sheets. *Proc. R. Soc. Lond. A* **253**, 313 (1959).
- Debrégeas, G., de Gennes, P. G. & Brochard-Wyart, F. The life and death of “bare” viscous bubbles. *Science* **279**, 1704–1707 (1998).
- Weaire, D. & Hutzler, S. *The Physics of Foams* 144–150 (Clarendon Press, 1999).
- Angenent, L. T., Kelley, S. T., St Amand, A., Pace, N. R. & Hernandez, M. T. Molecular identification of potential pathogens in water and air of a hospital therapy pool. *Proc. Natl Acad. Sci. USA* **102**, 4860–4865 (2005).
- Wu, J. Evidence of sea spray produced by bursting bubbles. *Science* **212**, 324–326 (1981).
- Woodcock, A. H., Kientzler, C. F., Arons, A. B. & Blanchard, D. C. Giant condensation nuclei from bursting bubbles. *Nature* **172**, 1144–1145 (1953).
- MacIntyre, F. Flow patterns in breaking bubbles. *J. Geophys. Res.* **77**, 5211–5228 (1972).
- Leifer, I., de Leeuw, G. & Cohen, L. H. Secondary bubble production from breaking waves: the bubble burst mechanism. *Geophys. Res. Lett.* **27**, 4077–4080 (2000).
- Jarvis, N. L., Garrett, W. D., Scheiman, M. A. & Timmons, C. O. Surface chemical characterization of surface-active material in seawater. *Limnol. Oceanogr.* **12**, 88–96 (1967).
- Culick, F. E. C. Comments on a ruptured soap film. *J. Appl. Phys.* **31**, 1128–1129 (1960).
- Pandit, A. B. & Davidson, J. F. Hydrodynamics of the rupture of thin liquid-films. *J. Fluid Mech.* **212**, 11–24 (1990).
- Debrégeas, G., Martin, P. & Brochard-Wyart, F. Viscous bursting of suspended films. *Phys. Rev. Lett.* **75**, 3886–3889 (1995).
- Brenner, M. P. & Gueyffier, D. On the bursting of viscous films. *Phys. Fluids* **11**, 737–739 (1999).
- da Silveira, R., Chaieb, S. & Mahadevan, L. Rippling instability of a collapsing bubble. *Science* **287**, 1468–1471 (2000).
- Savva, N. & Bush, J. W. M. Viscous sheet retraction. *J. Fluid Mech.* **626**, 211–240 (2009).
- Knelman, F., Dombrowski, N. & Newitt, D. M. Mechanism of the bursting bubble. *Nature* **172**, 261 (1954).
- Boulton-Stone, J. M. & Blake, J. R. Gas-bubbles bursting at a free-surface. *J. Fluid Mech.* **254**, 437–466 (1993).
- Zeff, B. W., Kleber, B., Fineberg, J. & Lathrop, D. P. Singularity dynamics in curvature collapse and jet eruption on a fluid surface. *Nature* **403**, 401–404 (2000).
- Duchemin, L., Popinet, S., Josserand, C. & Zaleski, S. Jet formation in bubbles bursting at a free surface. *Phys. Fluids* **14**, 3000–3008 (2002).
- Rayleigh, L. On the capillary phenomena of jets. *Proc. R. Soc. Lond.* **29**, 71 (1879).
- Kendall, J. M. Experiments on annular liquid jet instability and on the formation of liquid shells. *Phys. Fluids* **29**, 2086–2094 (1986).
- Blanchard, D. C. & Syzdek, L. Mechanism for the water-to-air transfer and concentration of bacteria. *Science* **170**, 626–628 (1970).
- Baylor, E. R., Baylor, M. B., Blanchard, D. C., Syzdek, L. D. & Appel, C. Virus transfer from surf to wind. *Science* **198**, 575–580 (1977).
- Farmer, D. M., McNeil, C. L. & Johnson, B. D. Evidence for importance of bubbles in increasing air-sea gas flux. *Nature* **361**, 620–623 (1993).
- Beerkens, R. G. C. & van der Schaaf, J. Gas release and foam formation during melting and fining of glass. *J. Am. Ceram. Soc.* **89**, 24–35 (2006).
- Handa, A., Emery, A. N. & Spier, R. E. On the evaluation of gas-liquid interfacial effects on hybridoma viability in bubble column bioreactors. *Dev. Biol. Stand.* **66**, 241–253 (1987).

Supplementary Information is linked to the online version of the paper at www.nature.com/nature.

Acknowledgements We thank P. Howell for discussions regarding our numerical simulations, and E. Villermaux and M. Brenner for feedback. We are grateful to the NSF via the Harvard MRSEC for support of this research.

Author Contributions J.C.B., L.C. and H.A.S. designed the research; J.C.B., R.d.R. and L.C. performed the research; J.C.B., R.d.R., L.C. and H.A.S. analysed the data; J.C.B. wrote the manuscript and all authors commented on it.

Author Information Reprints and permissions information is available at www.nature.com/reprints. The authors declare no competing financial interests. Readers are welcome to comment on the online version of this article at www.nature.com/nature. Correspondence and requests for materials should be addressed to J.C.B. (jbird@fas.harvard.edu) or H.A.S. (hastone@princeton.edu).

SUPPLEMENTARY INFORMATION

Further Details on Materials and Methods

Experimental methods

The soap bubble in Fig. 1A was made from a solution of water (50% by vol.), glycerol (45%) and Dawn brand dishwashing detergent (5%). A plastic syringe (30 cc) is filled with air and dipped into the soap solution so that a small amount of solution is collected on the tip (McMaster-Carr Type 304 Stainless Steel Dispensing Needle). The dispensing needle is then placed on to a clean glass slide, and the air is injected so that a hemispherical bubble forms on the glass slide. Approximately five seconds after the bubble is formed, the bubble is ruptured by contacting a dry stainless steel needle (McMaster-Carr 21 gauge dispensing needle) to the top, center of the bubble. Still images were collected using a fast camera (Phantom V7) before and a few seconds after rupture. Within the next minute, the lens of camera is changed to a higher magnification and focused on one of the smaller daughter bubbles (Fig. 1C). A dry needle (McMaster-Carr 30 gauge dispensing needle) is used to rupture the smaller bubble.

The interfacial bubble in Fig. 1E was made by injecting air into a sample of water collected from the Charles River, Cambridge, MA (42.369 N, 71.122 W). The water sample is placed in a Petri dish with a height between 2-3 centimeters. Air is injected under the water surface with a clean syringe, and the bubble is temporary stabilized by the indigenous surfactant. The bubble rupture occurs without assistance and is recorded with a Phantom V7 high-speed camera at 10,000 frames per second (see Supplementary Movie 1). The daughter bubbles are also filmed as they rupture on their own from gravitational draining (see Supplementary Movie 2).

The bubble in Fig. 2 was made from a moderately viscous (dynamic viscosity $\mu = 310$ cP) water-glycerol solution stabilized with 8.3 mM sodium dodecyl sulfate (SDS), which corresponds to the critical micelle concentration (1 CMC). A hemispherical bubble was formed on a clean glass slide using the same approach as the bubble in Fig. 1A. Synchronized high speed videos were captured with two Phantom V9 cameras, one recording the motion from the side and the other from the bottom through the glass slide (see Supplementary Movie 3).

The experiments reported in Fig. 4 were conducted using multiple bubble solutions. We injected different gases (air, nitrogen, carbon-dioxide, and helium) into solutions of silicone oil, water-glycerol, and water from the Charles River. The diameters of the bubbles ranged from 2 to 22 millimeters.

Silicone oil

The silicone oil (Dow Corning Corporation 200[®] fluid) was placed in a Petri dish with a depth of 2-3 centimeter. Air was injected with a syringe to form bubbles. These bubbles were created without surfactant, requiring that we used a sufficiently high

viscosity so that the bubble can be completely formed before it ruptures. The dynamic viscosities of the silicone oil ranged from $\mu = 4,900$ to $970,000$ cP (5,000 to 1,000,000 cSt) while the surface tension remained constant ($\gamma = 21$ to 22 mN/m). Experiments with lower viscosity silicone oils were attempted, but large, stable bubbles could not be created. The rupture of a 1,000,000 cSt bubble is shown in Supplementary Movie 5.

Water-glycerol

Different volume percentages of water-glycerol mixtures (50/50 to 5/95) were created such that dynamic viscosity ranged from 4.3 cP to 310 cP (surface tension $\gamma = 41$ to 55 mN/m). In addition, 8.3 mM of SDS surfactant (1 CMC) was added to the solution. The viscosities of these solutions at room temperature were obtained using a cone/plate geometry (40 mm diameter, 4°) on a Bohlin C-VOR rheometer. The densities were estimated from the densities of water and glycerol, and the surface tensions were determined with pendant drop tensiometry. The bubbles were blown using a syringe onto a clean glass slide. The syringe was connected to a gas cylinder containing either carbon-dioxide, nitrogen, or helium.

Local river water

A sample of water was collected from the Charles River, Cambridge, MA (42.369 N, 71.122 W). The water sample was placed in a Petri dish with a height between 2-3 centimeters. Either air or helium was injected under the water surface using a syringe, and the bubble was temporary stabilized by the indigenous surfactant. The rupture of one of these bubbles is shown in Supplementary Movie 6.

Typical experimental values and scaling

Film retraction

The speed of a retracting film that is regulated by inertia (rather than viscosity) scales as $U_I \propto \sqrt{\gamma/(\rho h)}$ ^{1,2}. Therefore the time for retraction to travel the length of the film scales as $\tau_I \propto \sqrt{\rho R^2 h/\gamma}$. A bubble with radius $R = 5$ mm, film density $\rho = 10^3$ kg/m³, film thickness $h = 10$ μ m, and surface tension $\gamma = 55$ mN/m will collapse on the order of 2 ms. This time is consistent with the collapse time of the bubble in Fig. 2a.

The speed of a retracting film that is regulated by viscosity (rather than inertia) is not constant, but rather increases exponentially with the characteristic rise time $\tau_v \propto \mu h/\gamma$ ^{3,4}. Therefore the characteristic velocity of viscous retraction over the length scale of the bubble is $U_v = R/\tau_v \propto \gamma R/(\mu h)$. The cross over between these two regimes occurs when the two characteristic velocities are on the same order $\sqrt{\gamma/(\rho h)} \approx \gamma R/(\mu h)$, or when $\frac{\rho \gamma R}{\mu^2} \frac{R}{h} \approx 1$. For a 5-mm bubble of silicone oil ($\gamma = 21$ mN/m), the transition

would occur when the dynamic viscosity μ is on the order of 7000 cP. The viscosities of the bubbles in Fig. 4 that distinguish the transition between daughter bubbles and no daughter bubbles are 5000 cP and 10,000 cP respectively.

In the inertial regime, the equation for the film velocity, $U_I \propto \sqrt{\gamma/(\rho h)}$, can be rearranged to $Ca \propto R/h \text{Re}^{-1}$. Here the capillary number is defined as $Ca \equiv \mu U/\gamma$ and the Reynolds number is defined as $\text{Re} \equiv \rho UR/\mu$. In the viscous regime, the equation for the film velocity $U_V \propto \gamma R/(\mu h)$ can be rearranged to $Ca \propto R/h$. Both of these scalings are consistent with our data in Fig. 4.

Torus breakup and daughter bubble formation

The images of the daughter bubble formation in Fig. 2b depict two concentric annular tori films pinching off into elongated bubbles and retracting on a timescale of approximately 50 ms. The radius of the tori is approximately $a = 100$ μm , the dynamic viscosity of the film is $\mu = 310$ cP, the surface tension is $\gamma = 55$ mN/m, and the distance the elongated bubbles retract is approximately $L = 1$ mm. The capillary driving force scales as $F_C \propto a\gamma$, where a is the radius of the torus. The viscous force resisting the relaxation scales as $F_V \propto \mu \frac{U}{h} A$, where μ is the dynamic viscosity, U is the characteristic relaxation velocity, h is the film thickness, and A is the characteristic area over which the viscous pressure acts. The relaxation time scales as $\tau = L/U$ and the viscous pressure acts over the cross-sectional area $A \propto h\sqrt{aL}$. Balancing the driving and resistive forces we find that $\tau = \frac{\mu L}{\gamma} \left(\frac{L}{a}\right)^{1/2} \approx 20$ ms. Therefore the timescale for the elongated bubbles to retract is consistent with a capillary-driven phenomenon regulated by viscosity.

Numerical methods

The film dynamics are simulated using an axisymmetric Cosserat-type model. We describe the essential features of the model here, and will publish the details and validation of this model elsewhere (Bird et al., in preparation). Our model tracks the position and velocity of elements of the fluid on the film as they stretch and retract. For simplicity, we describe this process for a planar curved film. The same steps are used to model axisymmetric geometries, although the calculations are slightly more involved.

The framework for our simulations is depicted in Fig. S1. The film is discretized into nodes connected by segments. Each segment has an effective length, Δs , and thickness h . Our model requires that each element conserves mass; so if the film segment stretches, the thickness decreases, and if the segment retracts, the segment thickness increases (Fig. S1a). Provided that the density ρ does not vary with time, the mass conservation statement is equivalent to the conservation of cross-sectional area for the planar film. The thickness and length of each fluid element are related by the equation $h\Delta s(t) = h\Delta s(0)$, such that the cross-sectional area is constant for all time, t .

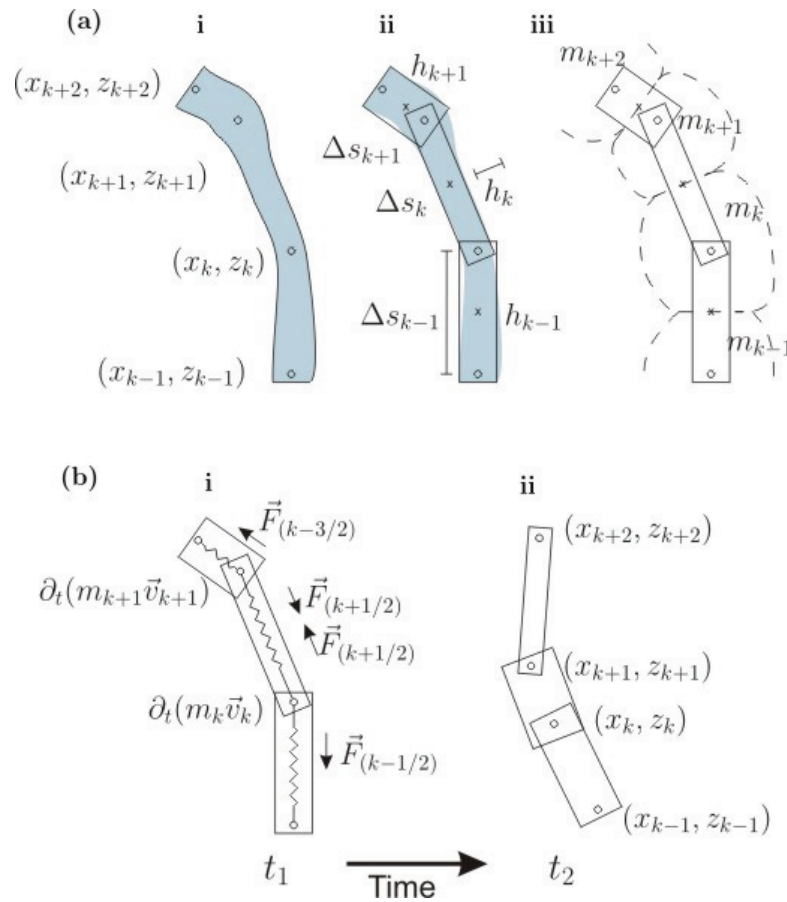


Figure S1. The framework for the Lagrangian thin film model. **(a)** The film is discretized into elements with thickness h and length Δs . If the film element stretches or contracts, the thickness adapts so that the effective mass m of each node is conserved. **(b)** (i) The surface and body forces of each element are computed, and the change in momentum is equal to the net force on each node. (ii) Stepping the system of ODEs forward in time updates the film shape.

Momentum is conserved by equating the change in momentum of the node with the net surface force around the node, $\frac{\partial}{\partial t}(m_k \vec{v}_k) = \vec{F}_{k+1/2} + \vec{F}_{k-1/2}$, where m_k and \vec{v}_k are the effective mass and velocity of the k^{th} node. Assuming any variations in thickness are negligible, the magnitude of the capillary force retracting each segment is $|\vec{F}_k| = 2w\gamma$, where w is the width of the film and γ is the interfacial tension on each side of the interface. Combined together, conservation of mass and momentum is satisfied when

$$\frac{\partial^2 \vec{X}_k}{\partial t^2} = \frac{2w\gamma}{m_k(0)} \left(\frac{\vec{X}_{k+1} - \vec{X}_k}{|\vec{X}_{k+1} - \vec{X}_k|} - \frac{\vec{X}_k - \vec{X}_{k-1}}{|\vec{X}_k - \vec{X}_{k-1}|} \right), \quad (1)$$

where \vec{X}_k denotes the position (x_k, z_k) . The evolution of the film shape is computed by numerically solving Equation 1 subject to the appropriate boundary conditions. As nodes near the retracting rim collide, the simulation considers these collisions as perfectly inelastic so as to model viscous dissipation in the rim. When calculating the shape of axisymmetric retracting films, the governing equation becomes slightly more complex. The width w is replaced by a function of the radius in both the mass and force terms and the second principle curvature adds an additional radial force inward. A detailed derivation and model verification will be published elsewhere.

Surface tension forces exert an inward pressure $\Delta P = 4\gamma/R$ on the initial hemispherical bubble, which is twice the pressure present in a submerged gas bubble because on the thin film bubble two surfaces need to be considered. Before rupture, the inner gas is confined within bubble and thus exerts an equal and opposite outward pressure on the film, often referred to as the Laplace pressure. When a hole is first formed in a hemispherical bubble, the time for the compressed air to equilibrate is approximately $t = R/c$, where c is the speed of sound. This time, 15 μs for a bubble with a 5 mm radius, is so much faster than the film retraction, $\sqrt{\rho R^2 h / \gamma} = 2$ ms, that we assume that the equilibration occurs instantaneously and model the gas as incompressible.

Without the outward Laplace pressure, capillary forces draw the bubble inward. As the bubble collapses, the inner gas escapes through the film hole and the volume inside the bubble decreases. The gas exerts a pressure back on the film, which we estimate using Bernoulli's principle. This pressure is significant when the film thickness is relatively thin, the gas density sufficiently high, and the hole in film relatively small (Fig. S2).

The pressure is added to our model in the following procedure. For each timestep, we calculate the change in volume inside the bubble. We assume that the gas does not compress, so that this change in volume is equivalent to the amount of inner gas that is displaced through the opening hole. Knowing the size of the hole, we compute the average velocity of the inner gas through the hole, V_g . As an order of magnitude approximation, we assume that the gas follows Bernoulli's equation, such that $P + \frac{1}{2}\rho V^2$ is constant along streamlines. Assuming that the pressure is homogeneous within the compressing bubble, the magnitude of the added pressure normal to the bubble surface is $\frac{1}{2}\rho_g V_g^2$, where ρ_g is the density of the inner gas. This pressure is added to the force balance in Equation (1) and updated each time step.

The pressure needed to displace the gas is relevant if it is near the same magnitude as the capillary pressure causing the bubble to collapse inward, $4\gamma/R$. Comparing these two pressures, and noting that V_g roughly scales with the approximate inward speed of the bubble $\sqrt{\gamma/\rho h}$, we find that the inner gas affects the shape when

$\frac{\rho_g}{\rho} \frac{R}{h} \geq O(1)$. Using representative values from our experiments, we find that

$\frac{\rho_g}{\rho} \frac{R}{h} = \frac{1}{10^3} \frac{10^{-2}}{10^{-5}} \approx 1$. The observed bubble collapse and the corresponding simulation

are depicted in Supplementary Movie 3 and 4 respectively.

Effects of inner gas

In the mechanism described in our paper, one of the rings of bubbles is formed when gas is trapped between the bottom interface and the collapsing film. The simulations suggest that the volume of gas trapped will decrease as the density of the gas increases due to the decrease in the radial translation of the film (Fig. S2). The implication is that the larger volume of trapped gas will lead to larger outer ring of daughter bubbles.

To test this prediction, we conducted a set of experiments, 55 hemispherical bubbles (95% glycerol, 5% water, stabilized by 1 CMC of SDS) are filled with helium, nitrogen, or carbon dioxide gas (details to be published elsewhere). The initial radii of the bubbles, R , vary between 1.5 and 6.2 mm. Indeed, the mean radius of the daughter bubbles formed between the interface and the film, r , decreases with increasing inner-gas density. For helium gas ($\rho_g = 0.17 \text{ kg/m}^3$), the average normalized daughter bubble size was $\langle r/R \rangle = 0.12$ with a standard deviation $\sigma = 0.02$. Increasing the density of the inner gas with nitrogen ($\rho_g = 1.2 \text{ kg/m}^3$), decreased the average bubble size to $\langle r/R \rangle = 0.08$ with a standard deviation $\sigma = 0.01$. Increasing the density more using carbon dioxide ($\rho_g = 1.8 \text{ kg/m}^3$), decreased the average bubble size to $\langle r/R \rangle = 0.07$ with a standard deviation $\sigma = 0.01$. Pilot data using sulfur hexafluoride ($\rho_g = 6.1 \text{ kg/m}^3$) resulted in an outer ring of even smaller bubbles. Therefore, the density of the gas inside the bubble does not affect the number of rings, yet does influence the average size of the daughter bubbles within the rings.

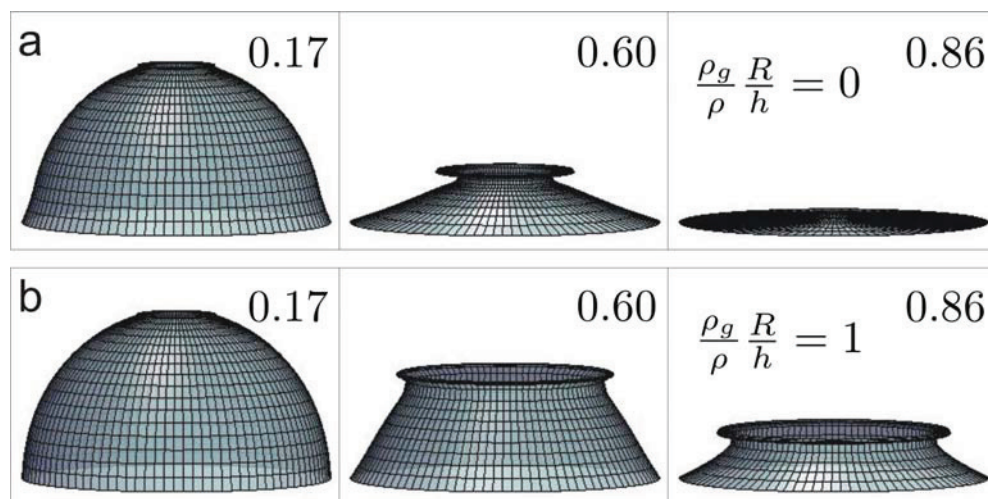


Figure S2. The effect of the internal gas density on the shape of the retracting film. **(a)** When the effects of the inner gas are neglected, the film rim travels radially inward to the point where it nearly reconnects. **(b)** When the effects of the inner gas are considered, the shapes of the retracting film are more similar to those observed in the experiments. The number in the upper-right corner of each image denotes the dimensionless time, $t/\sqrt{\rho R^2 h/\gamma}$.

-
1. Taylor, G. I. The dynamics of thin sheets of fluid III. Disintegration of fluid sheets. *Proc. R. Soc. London, Ser. A* **253**, 313 (1959).
 2. Culick, F. E. C. Comments on a ruptured soap film. *J. Appl. Phys.* **31**, 1128-1129 (1960).
 3. G Debrégeas, G., Martin, P. & Brochard-Wyart, F. Viscous bursting of suspended films. *Phys. Rev. Lett.* **75**, 3886-3889 (1995).
 4. Savva, N. & Bush, J. W. M. Viscous sheet retraction. *J. Fluid Mech.* **626**, 211-240 (2009).